https://doi.org/10.1007s00603-020-02227-8

ORIGINAL PAPER

Coupled Thermo–Hydro–Mechanical Modeling of Hydro-Shearing Stimulation in an Enhanced Geothermal System in the Raft River Geothermal Field, USA

Yilong Yuan[1,2] · **Tianfu Xu**[1] · **Joseph Moore**[3] · **Hongwu Lei**[4] · **Bo Feng**[1]

Abstract

The Raft River Enhanced Geothermal System (EGS) demonstration project aims to improve the geothermal production by enhancing the reservoir permeability via shear stimulation in well RRG-9. In this paper, we performed a series of 3D thermo–hydro–mechanical (THM) simulations to investigate the influence of hydraulic and thermal effects on the development of this EGS. The model includes synthetic fracture populations based on borehole televiewer images and in-situ stress measurements from well RRG-9. Fracture permeability evolution is determined using an empirical permeability law developed from laboratory experiments. The model was calibrated by comparing the hydraulic response to field observations, including wellhead pressure, injection rate, and well injectivity. Particularly, we analyzed the enhancement of reservoir permeability and the spatial extent of the stimulation zone for the given injection schedule. Our results indicate that the permeability enhancement of fractured geothermal reservoir is caused by the combined effects of injection-induced cooling and fluid pressure increase. The decrease of temperature plays a dominant role in reactivation of natural fractures under the hydro-shearing mechanism, while the higher injection pressure promotes shear failure and enlarges the stimulation zone. For the specified extensional stress state, the model favors greatest permeability enhancement along the maximum horizontal principal stress, a moderate vertical enhancement, and a smaller gain along the minimum horizontal principal stress.

Keywords Enhanced geothermal system · Hydro-shearing · Raft river geothermal field · Thermo-hydro-mechanical modeling · TOUGH2Biot

List of Symbols

M^{κ}	Mass accumulation (kg/m^3)
M^{θ}	Energy accumulation (J/m^3)
q^{κ}	Sink/source terms (kg/m^3 or J/m^3)
ϕ	Porosity (dimensionless)
ρ_{β}	Density of phase β (kg/m^3)
ρ_{R}	Density of rock grain (kg/m^3)
T	Temperature (°C)
λ	Thermal conductivity [W/(°C m)]
k	Absolute permeability (m^2)
μ_{β}	Viscosity of phase β (Pa s)
$\mathbf{g}$	Gravitational acceleration (m/s^2)
w	Displacement (m)
β_{T}	Thermal expansion coefficient (1/°C)
ε	Normal strain (dimensionless)
σ	Normal stress (Pa)
b_i	Fracture aperture of ith group (m)
β_i	Fracture trend of ith group (°)
μ_{s}	Static friction coefficient (dimensionless)
$\Delta\kappa_{\max}$	Maximum permeability enhancement (dimensionless)
τ_{ex}	Excess shear stress (Pa)
μ_{d}	Dynamic friction coefficient (dimensionless)
α_{P}	Pore compressibility (1/Pa)
d_5	Shear displacement at 5% of the maximum permeability enhancement
κ	Component, w, i, g are water, salt, and gas

✉ Bo Feng
fengbo82@126.com

[1] Key Laboratory of Groundwater Resources and Environment, Ministry of Education, Jilin University, Changchun 130021, China

[2] Engineering Research Center of Geothermal Resources Development Technology and Equipment, Ministry of Education, Jilin University, Changchun 130026, China

[3] Energy and Geoscience Institute, University of Utah, Salt Lake City, UT 84108, USA

[4] Institute of Rock and Soil Mechanics, Chinese Academy of Science, Wuhan 430071, China

$\mathbf{F}^{\kappa}$	Mass flux [kg/(m^2·s)]
$\mathbf{F}^{\theta}$	Heat flux (W/m^2)
V	Volume (m^3)
S_{β}	Saturation of phase β (dimensionless)
X_{β}^{κ}	Mass fraction (dimensionless)
C_{R}	Specific heat of rock grain [J/(kg·°C)]
u_{β}	Internal energy per unit mass (J/kg)
h_{β}	Specific enthalpy of phase β (J/kg)
$k_{r\beta}$	Relative permeability of phase β (dimensionless)
P_{β}	Fluid pressure of phase β (Pa)
G	Shear modulus (Pa)
υ	Poisson's ratio (dimensionless)
K	Bulk modulus (Pa)
σ'	Effective normal stress (Pa)
ε_{V}	Bulk strain (dimensionless)
l_i	Fracture distance of ith group (m)
γ_i	Fracture dip of ith group (°)
c	Cohesion of rough fracture (Pa)
κ	The logarithmic value of permeability ($= \log_{10}(k)$)
d	Shear displacement (m)
K_{f}	Shear fracture stiffness (Pa/m)
ϕ_0	Initial porosity (dimensionless)
d_{95}	Shear displacement at 95% of the maximum permeability enhancement
β	Phase, A, G are aqueous and gas

1 Introduction

Geothermal energy is an environmental-friendly resource that has been increasingly recognized and exploited in recent decades (Clark et al. 2012). The geothermal energy stored at depths of 3–10 km with the temperature ranging from 150 to 650 °C (e.g., hot dry rock, HDR) is considered as valuable thermal energy resource (MIT 2006). Economic geothermal energy production from HDR requires a reservoir that has sufficiently high permeability, fracture density, and fractured surface area to act as an efficient heat exchanger (Jeanne et al. 2014). Because of the low porosity of the rock matrix and the poor connectivity of natural fractures in HDR, which must be improved artificially to increase the recovery efficiency of thermal energy. The engineered HDR is known as the enhanced geothermal system (EGS) (Pandey et al. 2018).

Since the EGS concept was initially proposed in the early 1970s, more than ten EGS projects have been or are being developed and tested in the world (Breede et al. 2013). The accumulated field observations revealed that deep rocks are always naturally fractured. In addition, many seismic events were detected when the injection pressure was significantly lower than the magnitude of the minimum principal stress (Xie and Min 2016). It was realized that shear failure of pre-existing fractures (particularly those critically stressed fractures) is the primary source of permeability enhancement and seismicity (Pine et al. 1984; Ito and Hayashi 2003; Majer and Peterson 2007; Jeanne et al. 2014; Rutqvist et al. 2015; Rinaldi et al. 2015). Consequently, one strategy for creating an EGS is to increase reservoir permeability by shear failure of pre-existing fractures in high temperature rocks associated with shear dilation, which is referred to as hydro-shearing (Kelkar et al. 2012; Rutqvist et al. 2015; Rinaldi et al. 2015; Xie and Min 2016). However, there is poor knowledge with respect to the mechanism of this shearing process, which is crucial for understanding the geothermal reservoir permeability evolution and managing the induced seismicity (Riahi et al. 2013; Rinaldi et al. 2015; Xie and Min 2016).

As hydro-shearing relates to a coupled thermo–hydro–mechanical (THM) processes, numerical simulation offers an effective method to understand the variation (e.g., fluid pressure, temperature, effective stress, and permeability) occurring in the reservoir associated with stimulation treatments. Rutqvist et al. (2002, 2011) coupled the geomechanical code FLAC^{3D} (Itasca 2009) with the geothermal reservoir simulator TOUGH2 (Pruess et al. 1999), forming TOUGH-FLAC, which became one of the most popular THM simulators and was widely used in geothermal fields. Rutqvist et al. (2015) constructed a THM model to investigate injection strategies and the resulting effects of cold-water injection upon the Geysers EGS demonstration project Rinaldi et al. (2015). employed the hydro-shearing mechanism and carried out a THM model to analyze the potential for injection-induced fracturing and reactivation of natural fractures with associated permeability enhancement. Xie and Min (2016) developed a generic model, based on the hydro-shearing concept, to estimate the location of shearing onset, the required pressure, and the overall shearing growth direction during EGS hydraulic stimulation. Dempsey et al. (2013) developed a new model to describe the shear stimulation process, which was implemented in the software code FEHM (Finite Element Heat and Mass transfer) and applied to the Desert Peak geothermal field Wang et al. (2016). performed a semi-analytical analysis in a coupled THM framework to study the effects of injection temperature and coefficient of thermal expansion on fracture permeability evolution. Recently, a discrete fracture network (DFN) model was developed for the Raft River EGS project to investigate the effects of the water injection, while the effect of thermal stress was not considered in the model (Bradford et al. 2017). However, there are still some disadvantages in the above mentioned THM simulations: (1) some by linking the existing commercial simulators, but lacking the internal consistency and limiting the code development because not available of the source code; (2) some simplified the mechanical process; and (3) some simplified the stress-dependent fracture permeability by upscaling.

In this paper, an empirical relationship derived from the hydro-mechanical coupled laboratory experiments was successfully integrated into the thermo-hydro-mechanical coupled code to describe the reservoir permeability evolution of the fractured rock during reservoir stimulation. Based on the stress state and rock properties representative for the Raft River EGS demonstration project, we present a series of three-dimensional (3D) coupled THM simulations to investigate the development of this EGS project. Cold water injection with the combined effects of thermal and hydraulic processes was modeled corresponding to shear stimulation operations undertaken in June 2013. The model was calibrated by comparing the hydraulic response to field observations, including wellhead pressure, injection rate, and well injectivity. The main goal of this work is to understand the development of the EGS and the role of mechanical stress transfer caused by hydro- and thermo-mechanical stress perturbations due to the injection of cold water. In particular, the coupling model is aimed at predicting the enhancement of reservoir permeability and the spatial extent of the stimulation zone.

2 Numerical Method

2.1 Governing Equations for THM Processes

The coupled THM analysis was conducted using TOUGH2Biot (Lei et al. 2014, 2015), a novel THM simulator coupled with the extended 3D Biot consolidation model (Jaeger et al. 2007) into the non-isothermal, multi-component, multi-phase transport model TOUGH2 (Pruess et al. 1999). Comparing with the TOUGH-FLAC, the mechanical process in TOUGH2Biot is embedded into each time step, thus external data exchange is not necessary. As a consequent, the computation ability of TOUGH2Biot is more efficient. In addition, TOUGH2Biot can be easily extended for considering the THM coupled processes in fractured media (Lei et al. 2014, 2015).

The TOUGH2 code provides a reliable and open source base to simulate the thermal (*T*) and hydraulic (*H*) processes in subsurface flow system. The general formulations for multiphase flow and heat convection and conduction processes are summarized in Table 1 (see Nomenclature for definitions of all symbols used). More details can be found in Pruess et al. (1999).

The mechanical model assumes that a rock can move as an elastic material and obeys the generalized version of Hooke's law. Based on the stress equilibrium equations, compatibility equations, and the stress–strain relationships, the commonly-used Biot consolidation model can be obtained by combining the effective stress law with displacements (e.g., w_x, w_y, and w_z) as the primary unknown variables. Considering temperature effects, the extended Biot mechanical model is formulated, as shown in Table 2 (Lei et al. 2015).

2.2 Permeability Evolution of the Fractured Rock

Several mathematical models have been proposed for describing the permeability evolution of geothermal reservoir during fluid injection, such as thermo-poroelastic deformation of a regular array of fractures (Bai et al. 1999), shear-dilation of a statistically representative fracture population

Table 1 General mathematical model of coupled TH processes in TOUGH2

Description	Governing equations
Mass and energy conservation	$\frac{\mathrm{d}}{\mathrm{d}_t}\int\limits_V M^\kappa \mathrm{d}V = \int\limits_\Gamma \mathbf{F}^\kappa \cdot \mathbf{n}\mathrm{d}\Gamma + \int\limits_V q^\kappa \mathrm{d}V$
Mass accumulation	$M^\kappa = \sum\limits_{\beta=\mathrm{A,\,G}} \phi S_\beta \rho_\beta X_\beta^\kappa, \kappa = \mathrm{w,\ i,\ g}$
Mass flux	$\mathbf{F}^\kappa = \sum\limits_{\beta=\mathrm{A,\,G}} -k\frac{k_{r\beta}\rho_\beta}{\mu_\beta} X_\beta^\kappa \left(\nabla P_\beta - \rho_\beta \mathbf{g}\right)$
Energy accumulation	$M^\theta = (1-\phi)\rho_R C_R T + \sum\limits_{\beta=\mathrm{A,\,G}} \phi S_\beta \rho_\beta u_\beta$
Heat flux	$\mathbf{F}^\theta = -\lambda \nabla T + \sum\limits_{\beta=\mathrm{A,\,G}} h_\beta \mathbf{F}_\beta$

Table 2 3D extended Biot mechanical model

Description	Governing equations
Stress balance (Displacement)	$-G\nabla^2 w - \frac{G}{1-2\upsilon}\nabla(\nabla \cdot w) + \nabla P_\mathrm{a} + 3\beta_\mathrm{T} K \nabla T + F = 0$
Normal strain	$\varepsilon = \nabla w$
Normal stress	$\sigma' = \sigma - P = 2G\left(\frac{\upsilon}{1-2\upsilon}\varepsilon_\mathrm{V} + \varepsilon\right) + 3\beta_\mathrm{T} K \nabla T$

(Hossain et al. 2002; Dempsey et al. 2013), a crack-tensor approach that yields upscaled permeability (Rutqvist et al. 2015), and permeability as a function of the normal-stress dependent fracture aperture (Rinaldi et al. 2015). In this work, an empirical relationship derived from the hydro-mechanical coupled laboratory experiments and combined with the Mohr–Coulomb failure criterion was used to evaluate the permeability enhancement during reservoir stimulation.

2.2.1 Calculation of Fracture Permeability

To enable more sophisticated assessments, some representation of the natural fracture system in HDR was required. In this study, the synthetic fracture populations are mainly based on borehole televiewer images, which were used to represent the natural fracture system. As a consequence, many imaginary fractures (not discrete fractures) exist in each grid of the model. The permeability calculation on the strike-dip plane of each fracture is converted to the permeability tensor, which is defined by Eq. (1) (Zhou 2007). The nine permeability components resulting from Eq. (1) are different for each grid, which are resolved in the global frame (e.g., k_x, k_y, and k_z) to represent the equivalent permeability of the fractured media.

$$K = \sum_{i=1}^{n} \frac{b_i^3}{12 l_i} \begin{bmatrix} 1 - \cos^2\beta_i \sin^2\gamma_i & -\sin\beta_i \sin^2\gamma_i \cos\beta_i & -\cos\beta_i \sin\gamma_i \cos\gamma_i \\ -\sin\beta_i \cos\beta_i \sin^2\gamma_i & 1 - \sin^2\beta_i \sin^2\gamma_i & -\sin\beta_i \sin\gamma_i \cos\gamma_i \\ -\cos\beta_i \sin\gamma_i \cos\gamma_i & -\sin\beta_i \sin\gamma_i \cos\gamma_i & 1 - \cos^2\gamma_i \end{bmatrix} \tag{1}$$

2.2.2 Enhancement of Fracture Permeability

Changes in fluid pressure and temperature result in the alteration of a rock's local stress, which could induce shear failure along an existing fracture plane (Dempsey et al. 2013) Lee and Cho's (2002). laboratory experiments demonstrated that shear dilation occurs until shear displacement reaches a maximum value. As a result, fracture permeability is increased due to an increase in mechanical aperture caused by shear dilation during shear displacement (Fig. 1).

Generally, the stress state acting on a fracture plane is very important to determine the shear failure potential of the specified rough fracture. Based on Xie and Min (2016), the effective normal stress, σ_n' and shear stress, τ_n acting on a given fracture plane are related as follows:

$$\sigma_n' = \sigma_x' l^2 + \sigma_y' m^2 + \sigma_z' n^2 \tag{2}$$

$$\tau_n = \left[\left(\sigma_x' - \sigma_y'\right)^2 l^2 m^2 + \left(\sigma_y' - \sigma_z'\right)^2 m^2 n^2 + \left(\sigma_z' - \sigma_x'\right)^2 l^2 n^2 \right]^{1/2}, \tag{3}$$

where l, m and n are the direction cosines of the fracture plane normal with respect to the principal stress axes σ_x', σ_y' and σ_z', respectively.

The Mohr–Coulomb failure criterion was used to define the shear strength of the fractured rock, written as:

$$F_c = \left|\tau_n\right| - \mu_s \sigma_n' - c \tag{4}$$

Based on Eq. (4), $F_c > 0$ means that the stress state acting on a fracture plane satisfies the shear failure criterion. As a result, the hypothetical shear displacement is evaluated based on the static/dynamic friction model as given below (McClure and Horne 2012):

$$d = \frac{\tau_{ex}}{K_f}, \begin{cases} \tau_{ex} = 0 & \text{for} F_c < 0 \\ \tau_{ex} = \left|\tau_n\right| - \mu_d \sigma_n' & \text{for} F_c \geq 0 \end{cases} \tag{5}$$

Using the data from hydro-mechanical laboratory experiments by Lee and Cho (2002), an empirical model for the increase in rough fracture permeability associated with shear displacement is given as (Dempsey et al. 2013):

$$\Delta\kappa = \frac{\Delta\kappa_{max}}{1 + \exp\left[\ln(19) \cdot \left(1 - 2.0 \frac{d - d_5}{d_{95} - d_5}\right)\right]} \tag{6}$$

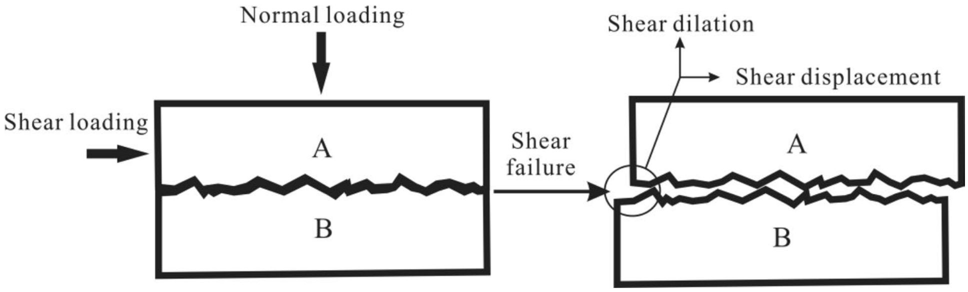

Fig. 1 Schematic diagram of shear dilation during failure for a rough fracture

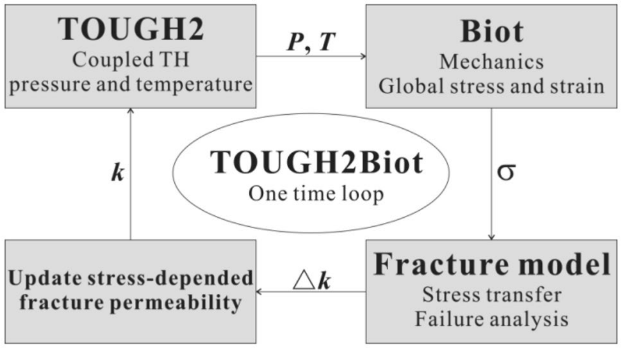

Fig. 2 Coupling THM processes for updating stress-dependent fracture permeability

Based on Eqs. (1–6), permeability evolution of a fractured geothermal reservoir associated with cold water injection could be evaluated.

2.3 Method for Coupling THM Processes

TOUGH2Biot inherits the fully coupled TH processes from TOUGH2. Displacements, stress, and strain can be obtained by solving the extended mechanical equations. In one-time loop of sequential calculation (Fig. 2), fluid pressure (P), temperature (T), and phase saturation (S) are calculated by TOUGH2 firstly. Then these variables are used by the mechanical model as the known variables for mechanical solution (e.g., displacement, stress, and strain). The mechanical process gives feedback to the flow through the stress-dependent fracture permeability (discussed in Sect. 2.2). The details and the model architecture of TOUGH2Biot have been reported in our previous work (Lei et al. 2014, 2015). The reliability of TOUGH2Biot was verified against two 1D analytical solutions and by comparing with other THM simulators (Lei et al. 2014, 2015).

3 Model Setup of Raft River Geothermal Field

3.1 Description of Raft River Geothermal Field

The Raft River geothermal field is located in southern Idaho (Fig. 3a). It is owned and operated by U.S. Geothermal Inc. and produces approximately 11 MWe from a binary power system (Bradford et al. 2013; Plummer et al. 2014, 2015).

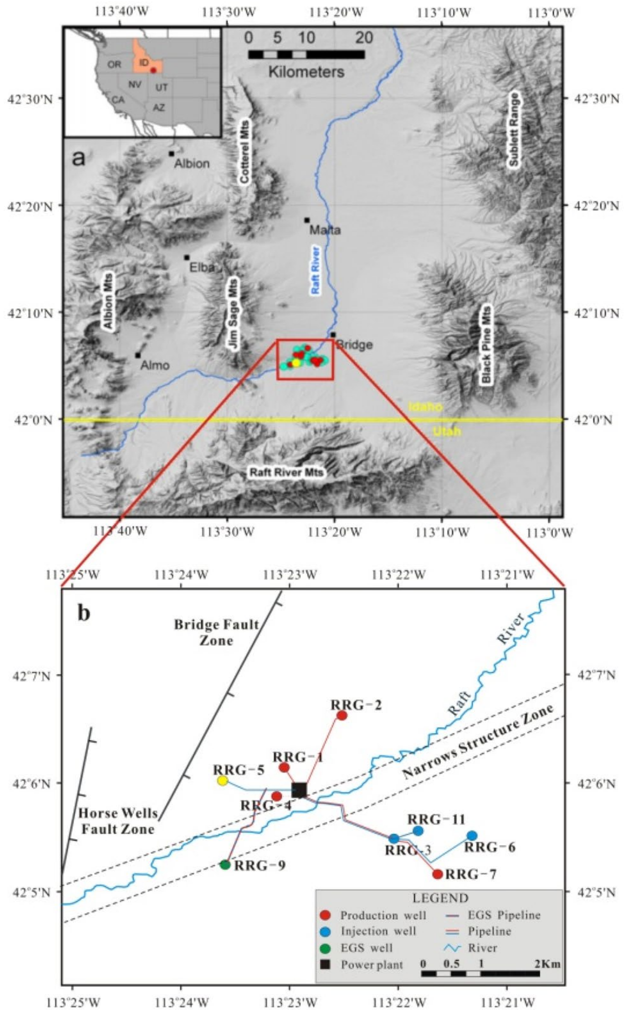

Fig. 3 **a** Location and physiographic setting of the Raft River geothermal field; **b** locations of geothermal wells, pipelines, and inferred structural features (Ayling et al. 2013; Bradford et al. 2015)

The geologic structure in the Raft River geothermal area has been extensively studied using geophysical methods, surface mapping, and core lithologic descriptions of subsurface core materials (Bradford et al. 2013; Plummer et al. 2015). Two major fault zones have been identified on the west side of this field, the Bridge and Horse Wells Fault Zones (Diek et al. 2012; Bradford et al. 2013). Both zones strike NNE-SSW (Fig. 3b). These listric faults dip 60°–80° to the east at the surface and become nearly horizontal in the Tertiary sediments. As a result, many near vertical fractures were created at the base of the sediments (Ayling et al. 2013; Plummer et al. 2014), as shown in Fig. 5.

Deep wells drilled into the geothermal system have encountered approximately 1500 m of discontinuous Quaternary and Tertiary volcaniclastic and volcanic rocks above the Precambrian metamorphic basement (Fig. 4). These Precambrian rocks host the geothermal reservoir with a thickness of 180 m and consist of schist, quartzite, and quartz monzonite (Bradford et al. 2013). The primary reservoir is the Elba Quartzite, which is fine-grained metamorphosed quartz-rich sandstone (Jones et al. 2011; Diek et al. 2012; Bradford et al. 2013). The temperature–pressure logs were conducted in four wells in this field, which demonstrates that

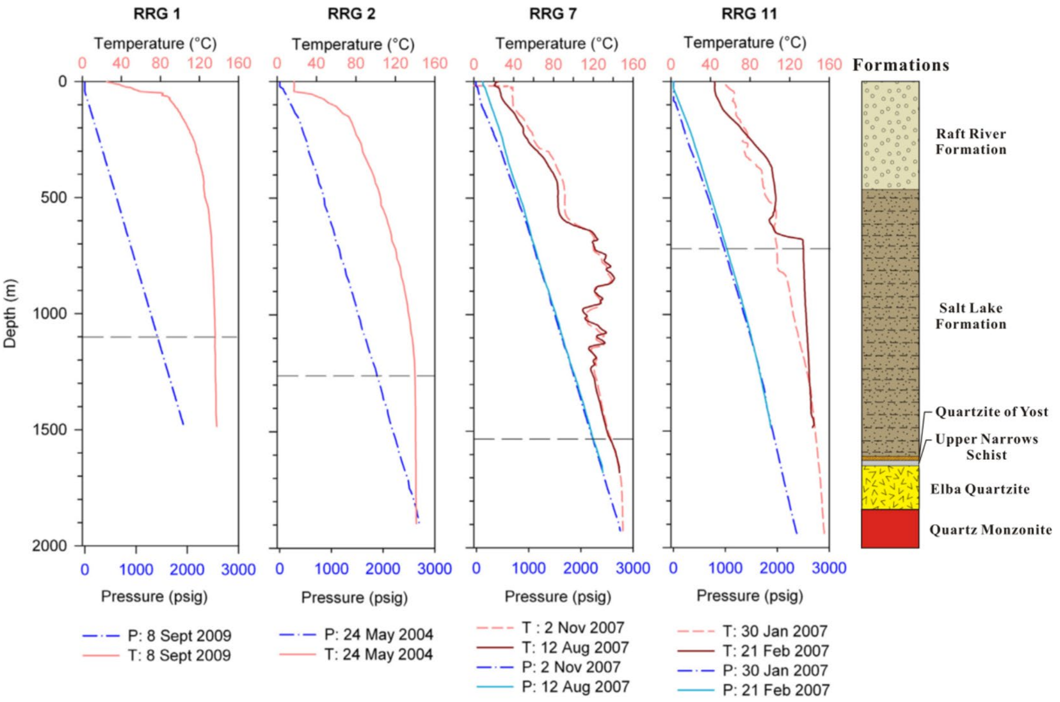

Fig. 4 Static pressure–temperature profiles in four deep geothermal wells with stratigraphic distribution at Raft River geothermal field. Dashed horizontal lines represent depth of casing for the well (Ayling et al. 2013; Bradford et al. 2013)

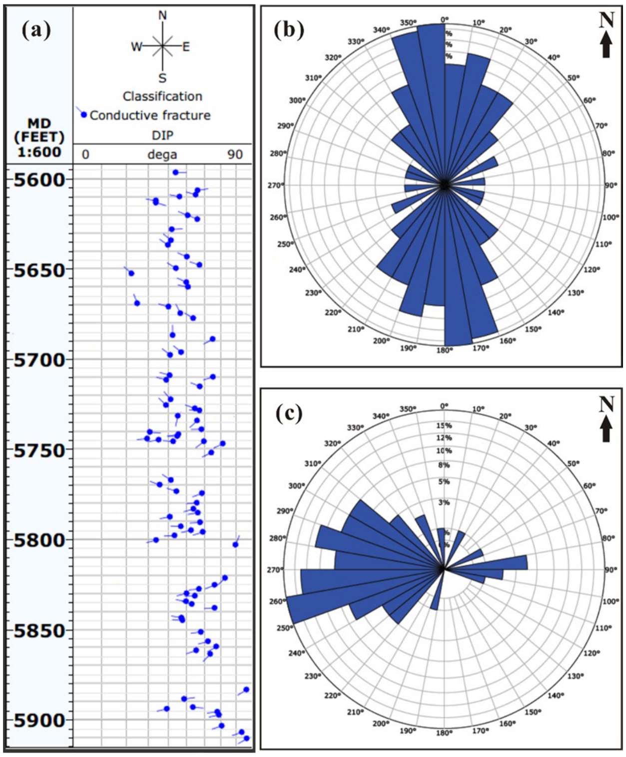

Fig. 5 Natural occurring fractures in well RRG-9 **a** tadpole diagram of identified fractures, **b** fracture population dip azimuths, and **c** fracture population dip strikes (modified from Bradford et al. 2013)

the temperature in the main reservoir unit is around 140 °C, as shown in Fig. 4.

The target well RRG-9 was completed at a measured depth (MD) of 1808.1 m in quartz monzonite (Jones et al. 2011; Diek et al. 2012; Bradford et al. 2013). Prior to setting the casing, a deviation survey and acoustic, gamma, SP, and density logs were run. After the well was cased and cemented, a borehole televiewer survey was conducted in the open-hole section between 1683.9 m and 1804.7 m MD. Eighty-six naturally occurring fractures that intersected the wellbore were identified (Fig. 5). The majority of these fractures are steeply dipping (e.g., 40°–60°) and strike to the northeast (Bradford et al. 2013, 2017). Additionally, a short-term injection test was conducted in February 2012 (shortly after the well was completed) to infer in-situ stress and for estimating the fracture opening pressure (details can be found from Bradford et al. 2013). After that, the well was shut in for approximately 1.5 years after the injection test to build a 10-inch pipeline connecting the well to the power plant and conduct required stimulation program in 2013 (Bradford et al. 2017).

Beginning June 13, 2013, a series of reservoir stimulation operations with varying injection pressures and temperatures were undertaken at well RRG-9 (Bradford et al. 2014; Plummer et al. 2014, 2015). As shown in Fig. 6a, the stimulation program is divided into three stages based on the wellhead pressures (WHPs): Stage I, from June 13 to August 22, 2013,

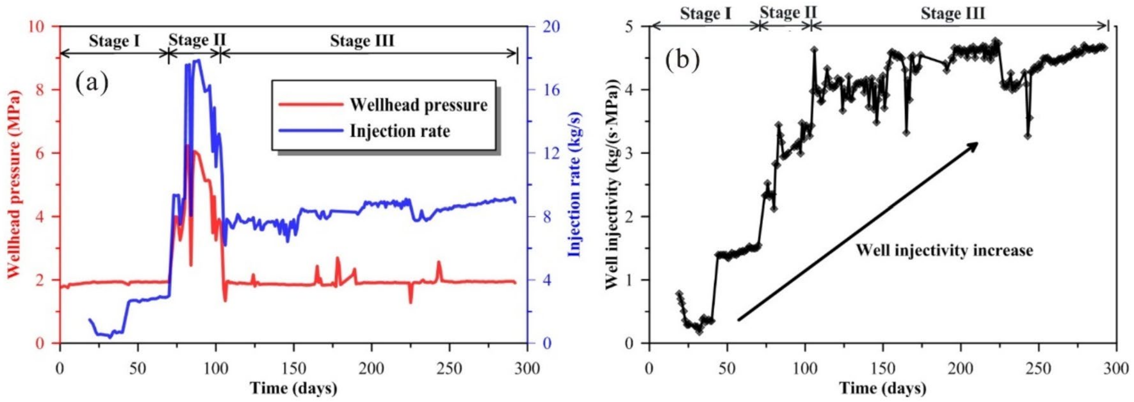

Fig. 6 Evolution of **a** wellhead pressure and injection rate, and **b** well injectivity during the field stimulation treatment in stages I, II, and III

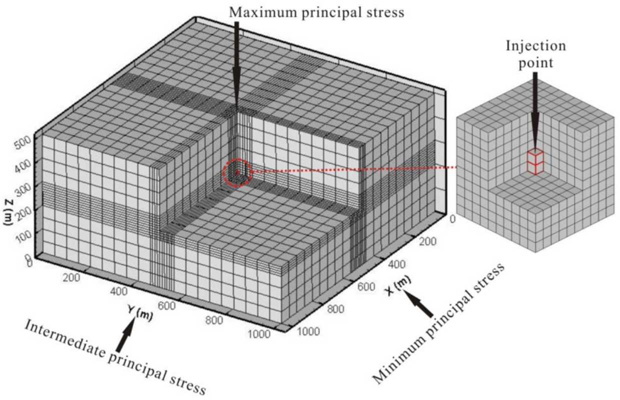

Fig. 7 Cut-away view of the computational grids, showing the high-resolution area, the location of injection well and perforated interval, and the principal stresses directions

the WHPs were maintained at 1.9 MPa, and the injection temperature at wellhead was ~ 40 °C; Stage II, from August 23 to September 24, 2013, the WHPs were high but changed between 3 and 6 MPa, and the injection temperature was ~ 43 °C in the first 17 days and ~ 13 °C in the later 13 days; Stage III, from September 25, 2013 to March 30, 2014, the WHPs were maintained at 1.9 MPa, and the injection temperature was ~ 29 °C. As a result, the well injectivity has consistently increased from 0.4 to 4.7 kg/(s MPa) (Fig. 6b).

3.2 Model Setup

3.2.1 Model Geometry and Spatial Discretization

The conceptual model of the fractured system was developed based on information provided by drilling logging data and borehole imaging results (Fig. 7). The top of the model is 1300 m below the land surface. The model geometry is 1 km × 1 km in the horizontal direction and 0.5 km in the vertical direction. The z-axis aligns with the maximum in-situ principal stress (σ_V). The *x*-axis and *y*-axis align with the intermediate (σ_H) and the minimum (σ_h) principal stress, respectively. The grid size in the central injection zone (100 m × 100 m × 100 m) is 10 m and increases to 50 m in the surrounding regions. The injection well with a radius of 0.1 m located in the center of the domain. Consistent with the field test results, the injection interval located in the Elba Quartzite reservoir with thickness of 20 m (Fig. 7).

3.2.2 Initial and Boundary Conditions

The initial reservoir temperature is assumed to be a uniform 140 °C, because the temperature measurements in Fig. 4 show an almost constant temperature at reservoir depth. The initial fluid pressure in the domain center is 15.24 MPa, which is equal to the original value obtained from the field (Diek et al. 2012). The pressure profile is specified in accordance with the hydrostatic pressure. The initial geomechanical conditions are extracted from Bradford et al. (2013). The vertical stress gradient is about $\sigma_V = 19$ MPa/km (0.84 psi/ft) corresponding to a bulk density of the overlying formations. The intermediate principal stress is oriented in the NNE-direction (*x*-axis, σ_H) with a gradient of 16.5 MPa/km (0.73 psi/ft). The minimum principal stress is oriented in the NWW-direction (*y*-axis, σ_h) with a gradient of 14 MPa/km (0.62 psi/ft).

To simulate the varied injection processes (Fig. 6), the time-variable Dirichlet boundary conditions are applied to the injection well. The friction pressure loss along the wellbore was neglected, which means the wellhead high pressure can be effectively conducted to the injection interval. Open flow boundaries were imposed on most edges of the model domain (i.e., constant pressure and temperature), while zero heat and mass flow boundary conditions were enforced on the bottom boundary. We imposed a restriction of zero-displacement normal to the bottom and lateral boundary surfaces, whereas the top boundary is allowed free to move freely.

3.2.3 Initial Permeability

The initial fracture patterns are based on borehole televiewer images in the open-hole section of well RRG-9 (see Fig. 5). Fracture density, tendency, and dips at different intervals are listed in Table 3.

The initial fracture aperture $b = 0.032$ mm was inferred through trial-and-error procedure by comparing the simulated and measured pressure profiles during the injection test undertaken in 2012 (see Sect. 3.3). Based on Eq. (1), the distribution of initial permeability k_x, k_y, and k_z are calculated and shown in Fig. 8. The fracture permeability calculation model implies that permeability anisotropy of the fractured geothermal reservoir is a function of all fracture orientations.

3.2.4 Reservoir Properties and Parameters

The reservoir properties of the model were based on those of the Elba Quartzite in RRG-9, as shown in Table 4. The values of density, Young's modulus and Poisson's ratio are determined from core samples analysis (Jones et al. 2011; Diek et al. 2012). The porosity value of the reservoir is taken from Freifeld's reservoir model (Freifeld 2011). The thermal conductivity and specific heat capacity of the rock are vital for the temperature changes during cold water injection, which are taken from Diek et al. (2012) and Bahrami et al. (2015). Thermal effects are also taken into account as well and the coefficient of liner thermal expansion is $\beta_T = 1.65 \times 10^{-5}$ °C^{-1} (Diek et al. 2012). The static and dynamic friction coefficients are chosen after the results of McGarr (1999) and Dempsey et al. (2013). Shear fracture stiffness is an elastic parameter and the application of Eq. (5) to an intact rock in the post-failure period may not yield the most correct relationship between stress changes and displacement. However, inserting Eqs. (5) into (6) shows that K_f affects the slope of the permeability-displacement curve, while the final magnitude is fixed by Δk_{max} alone. Considering the long-term stimulation program, shear displacements are finally greater than d_{95}, thus, the final control on permeability enhancement is based on Δk_{max}. Therefore, we use field observed data to constrain the value of Δk_{max} during reservoir stimulation (Dempsey et al. 2013). In addition, the parameters used in Eq. (6) (e.g., d_5 and d_{95}) is derived from the hydro-mechanical laboratory experiments by Lee and Cho (2002) and verified by Dempsey et al. (2013). The fracture cohesion is taken from Kelkar's model (Kelkar et al. 2012) and validated by matching the field observations.

Injection temperature at the location of the perforated interval was estimated by the wellbore simulator T2WELL (Pan et al. 2011), such as in stage I, the bottomhole

Table 3 Parameter values used for generating synthetic fractures

Depth (m)	Fracture density (1/m)	Probability of fracture tendency			Probability of fracture dip	
		70°–110°	250°–290°	Other	40°–60°	Other
1300–1400	0.2	0.3	0.3	0.4	0.6	0.4
1400–1500	0.4	0.3	0.3	0.4	0.6	0.4
1500–1600	0.9	0.3	0.3	0.4	0.6	0.4
1600–1700	0.4	0.3	0.3	0.4	0.6	0.4
1700–1800	0.2	0.3	0.3	0.4	0.6	0.4

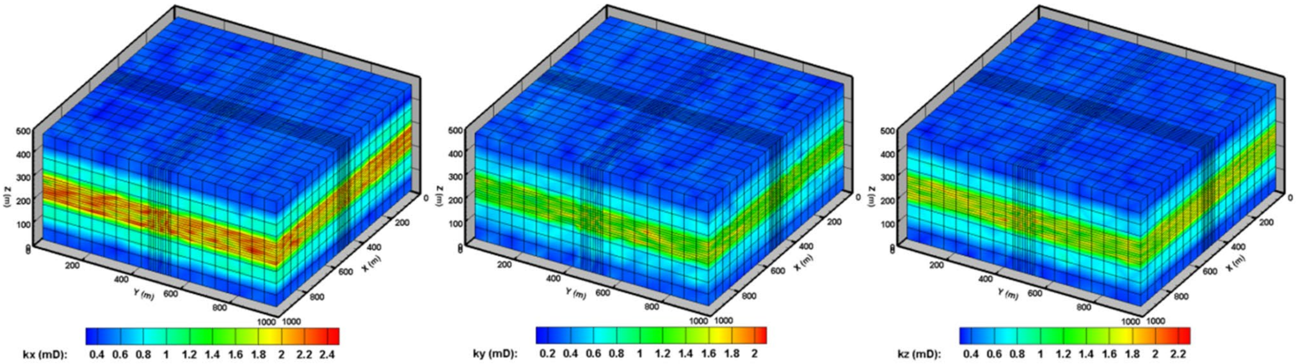

Fig. 8. 3D images display the spatial distribution of initial fracture permeability in *x*, *y*, and *z* directions, respectively

Table 4 Parameter values used in the present 3D THM model, with references given where available

Parameter	Value
Material	
Rock density (kg/m^3), ρ_R	2300 (Jones et al. 2011)
Porosity, ϕ	5% (Freifeld, 2011)
Thermal conductivity (W/m·°C), λ	4.0 (Diek et al. 2012; Bahrami et al. 2015)
Specific heat capacity (J/kg·°C), C_R	900 (Diek et al. 2012; Bahrami et al. 2015)
Thermal expansion coefficient (/°C), β_T	1.65×10^{-5} (Diek et al. 2012)
Young's modulus (GPa), E	15.8 (Jones et al. 2011)
Poisson's ratio, υ	0.15 (Jones et al. 2011; Diek et al. 2012)
Pore compressibility (/Pa), α_P	4.0×10^{-10} (Bahrami et al. 2015)
Fracture	
Static friction coefficient, μ_s	0.65 (Dempsey et al. 2013)
Dynamic friction coefficient, μ_d	0.55 (McGarr, 1999)
Cohesion (MPa), c	2.0 (Kelkar et al. 2012)
Shear fracture stiffness (MPa/m), K_f	500 (Bai et al. 1999)
Parameters used in Eq. (6)	
$\Delta\kappa_{max}$	1.7
d_5(mm)	1.5 (Lee and Cho 2002; Dempsey et al. 2013)
d_{95}(mm)	5 (Lee and Cho 2002; Dempsey et al. 2013)
Operational	
Injection depth (m)	1500 (Bradford et al. 2013)
Thickness of injection interval (m)	20 (Bradford et al. 2013)
Wellhead pressure (MPa)	Consistent with field data (see Fig. 6a)

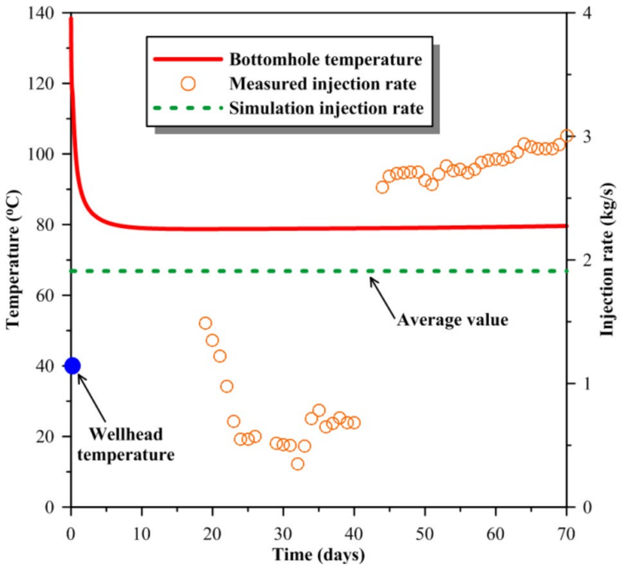

Fig. 9 Evolution of bottomhole temperature at well RRG-9 in Stage I

temperature was about 80 °C as a result of heat exchange with surrounding rocks (Fig. 9). In stage II, the temperature of injected water was ~ 43 °C in the first 17 days and ~ 13 °C in the later 13 days, and the injection rate was high but changed significantly. For simplicity, a constant bottomhole temperature of 50 °C was estimated and validated by matching the field observations. In stage III, the bottomhole temperature was assumed consistent with stage II, because the combined effects of (1) elevated injection temperature (~ 29 °C), (2) decreased injection rate, and (3) cooling of surrounding rocks.

3.3 Model Calibration

Model calibration is necessary for understanding whether the system is correctly responding to the injection of fluids and whether boundary and initial conditions are properly set (Rinaldi et al. 2015). The calibration here was made by simulating the injection test undertaken in 2012. According to Plummer et al. (2014, 2015), the injection rates were step-by-step increased from 0.66 to 13.25 kg/s and each rate lasted for about 30 min (Fig. 10). The step-rate tests provide a means of determining the overall permeability of the reservoir connected to well RRG-9, and how the system responds to increasing and decreasing injection pressure. Consequently, the model calibration can be used to determine the initial fracture aperture. The thermal conductivity, specific heat capacity, pore compressibility, and thermal expansion coefficient were calibrated as well, with the resulting values listed in Table 4, showing a good match between simulated and measured pressure profiles (Fig. 10).

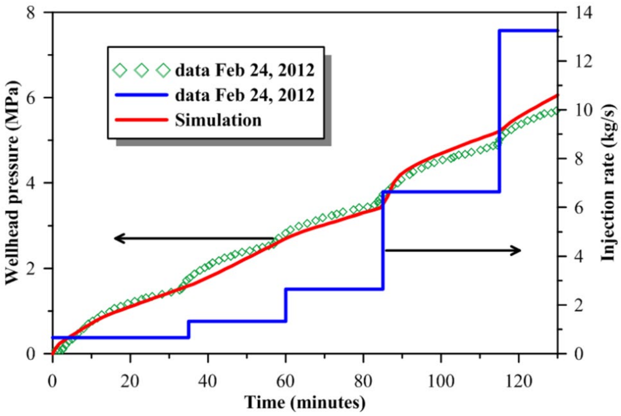

Fig. 10 Comparison of observed and simulated wellhead pressure changes in RRG-9 during the injection test undertaken in 2012. The solid blue line shows step-rate injection rates

4 Results and Discussion

4.1 History Matching of Field Injection Test

4.1.1 Stage I

As shown in Fig. 11a, the model results are able to reproduce the pattern of field measured injection rates. The modeled injection rates increased gradually, whereas the measured injection rates increased rapidly. This may be attributed to the quick failure of favorable fractures in the naturally fractured reservoir around the target stimulation well. In addition, the measured injection rates initially decrease due to the instability of the formation in the early injection period.

In detail, the evolution of the modeled injection rates under constant injection pressure and temperature in Stage I can be divided into four phases:

(1) In the first 20 days, the injection rates remain constant, which means that the initial permeability around the injection well has not yet been altered by cold water injection.

(2) Between 20 and 42 days, there appears a slight increase of injection rates, which then stabilizes at a value of 1 kg/s. To improve understanding the mechanism of permeability enhancement by shearing of pre-existing fractures associated with cold water injection. The specified fracture (e.g., *Fra*_1 with strike 201° and dip 48.5°) was choose to analyze the evolution process of fracture permeability enhancement. *Fra*_1 belongs to the control volume *Ele*_1 with 14 m horizontal distance from the injection well.

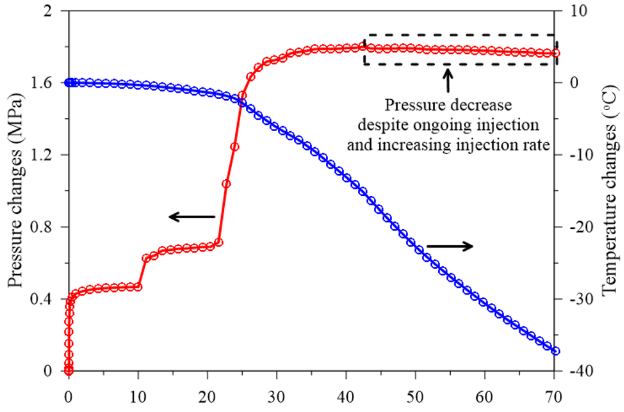

Fig. 12 Changes of pressure and temperature at element *Ele*_1 during the first 70 days stimulation program

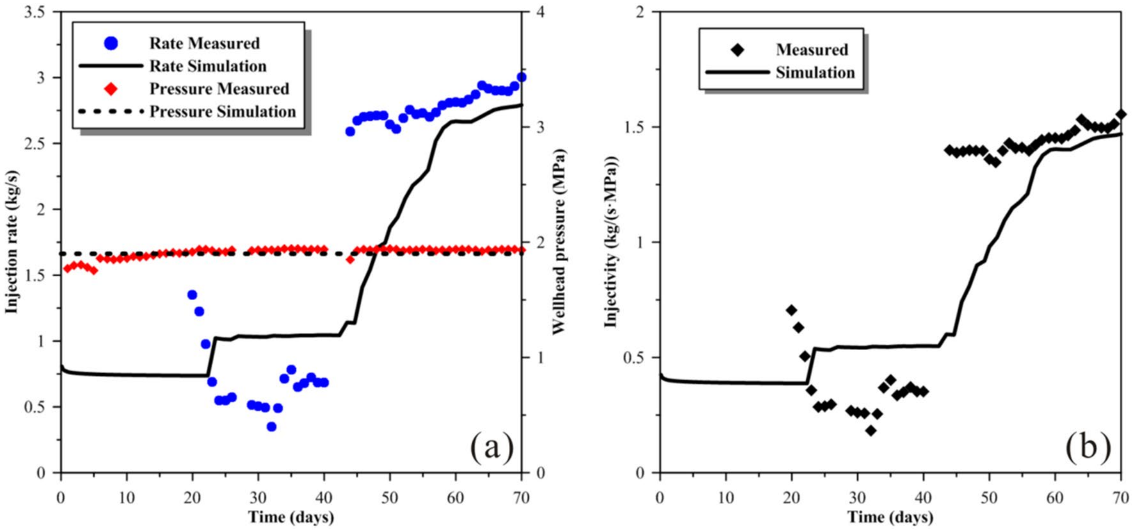

Fig. 11 Comparison of the modeled and measured **a** injection rates and wellhead pressures and **b** well injectivity in Stage I

Figure 12 shows the evolution of pressure and temperature changes at *Ele*_1 in stage I.

As shown in Fig. 12, due to injection of cold water leads to a decrease of reservoir temperature and an increase of pore pressure around the injection well, which leads to a decrease of effective stress in the reservoir. This can be represented by Mohr diagram and the movement of stress circles to demonstrate such a physical process, as shown in Fig. 13. The initial stress state on *Fra*_1 is represented by a point located within the area that is bounded by the biggest stress circle (Fig. 13a). As a result of thermal and hydraulic stresses changes, the stress state on *Fra*_1 has moved to the failure envelope on the 44th day (Fig. 13b). Consequently, *Fra*_1 suffers shear failure and enhances the permeability of grid *Ele*_1.

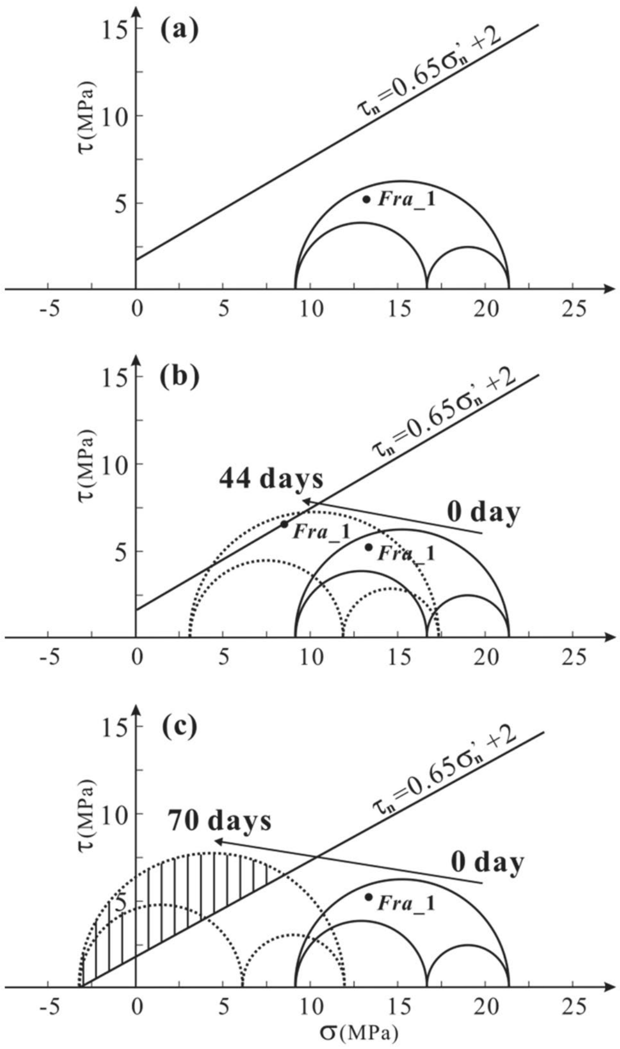

Fig. 13 Concept of hydro-shearing of pre-existing fractures, **a** initial stress state without thermal and hydraulic effects, **b** decrease in effective stress required to sliding of *Fra_1* on the 44th day, **c** stress state changes on the 70th day at *Ele*_1. The minus sign represents the tensile stress

(3) With the continued injection of cold water further decreases the reservoir temperature and increases the pore pressure deep into the reservoir, which leads to widespread failure of the fractured rock and permeability enhancement on the 43rd day. Consequently, the rapid growth of injection rates is observed (Fig. 11a). Obviously, the slope of injection rate is affected by the stress state, fracture patterns of pre-existing fracture systems, and the thermal properties of the rock. It is interesting that the pressure response switches from a steady increase to a slow decline despite ongoing injection with an increasing flow rate (Fig. 12b). This is because the stimulation front moves further into the reservoir. The region behind the stimulation front is more effective for conducting water to the far-field. Whether such an effect could be observed in the field tests remains an open question.

(4) After about 60 days, the injection rates tend to stabilize again. This is because the long distance of fluid traveling leads to increase of fluid temperature and decrease of pressure gradient, until a new balance is reached between stress state and fracture permeability. This phenomenon fits well with the field observations (Fig. 11). With the continuous injection and temperature decreases, the tensile stress appears around the injection well (i.e., the minus value of effective stress occurs in Fig. 13c). As for the shaded region in Fig. 13c, it represents all the fractures that would have been slid at the current stress state.

4.1.2 Stage II

In stage II, the injection pressure increases rapidly, and after peaks at 6.2 MPa on the 82th day, it decreases to 1.9 MPa on the 105th day (Fig. 14a). As shown in Fig. 14a, the injection rates follow the trend of the injection pressure, which increase from 7.3 kg/s on the 73rd day to 17.9 kg/s on the 89th day. It is noted that with sharp decrease of injection pressure from 89th day to 105th day, while well injectivity decrease merely slight (Fig. 14b). This is because the injection of cold water lowers the temperature in the reservoir and leads to shrinking of the rock matrix, which counteracts with the influence of the injection pressure decreases. After stimulation treatment in Stage II, the well injectivity quickly rises from 1.5 to 3.4 kg/(s MPa) within ~ 30 days (Fig. 14b). This is mainly because the elevated fluid pressures reduce the effective stress acting on a fracture plan, which promotes shear failure on pre-existing fractures.

4.1.3 Stage III

As shown in Fig. 15a, both the modeled and measured injection rates increase slightly, while the modeled injection rates

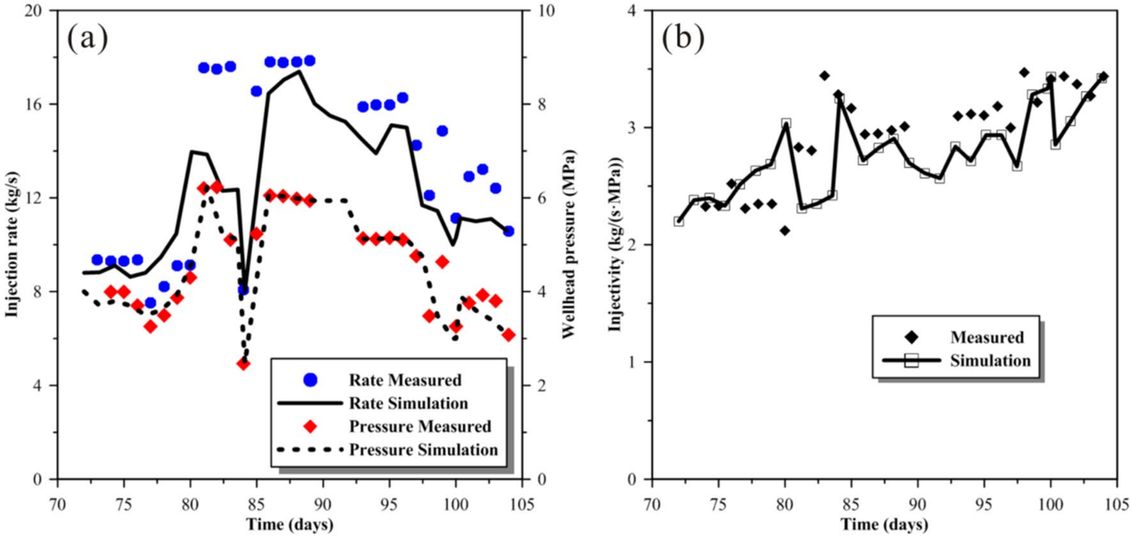

Fig. 14 Comparison of the modeled and measured **a** injection rates and wellhead pressures and **b** well injectivity in Stage II

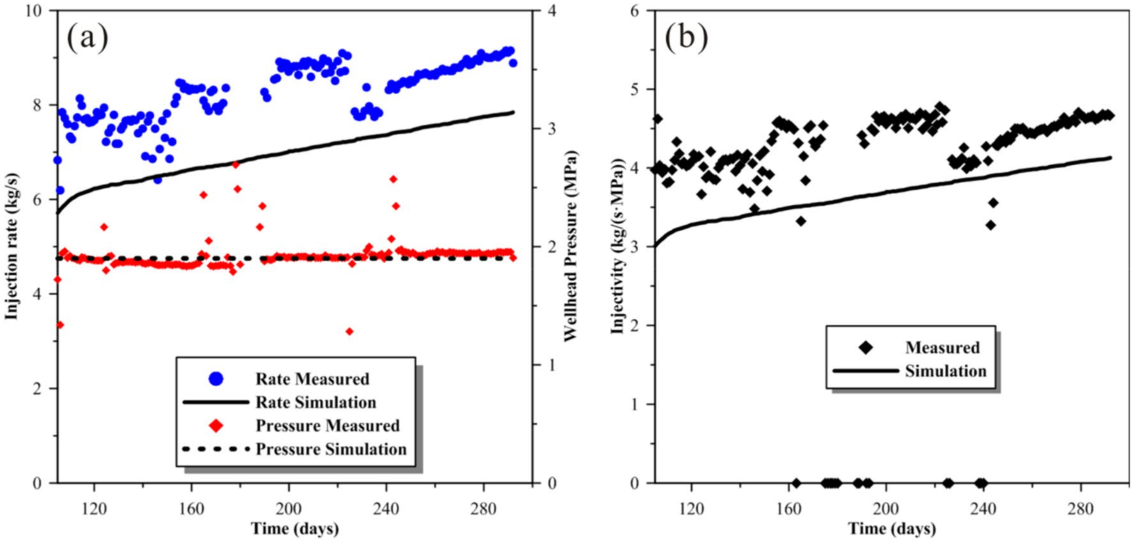

Fig. 15 Comparison of the modeled and measured **a** injection rates and wellhead pressures and **b** well injectivity in Stage III

are lower than the measured values. This is mainly because the distribution patterns of the naturally fracture system in our model cannot completely match with the field reservoir, especially the region where far from the target injection well (e.g., the synthetic fracture populations are mainly based on borehole televiewer images). Therefore, the difference between the simulated and measured values in stage III is significantly larger than that of stages I and II. In addition. the mild stimulation effects in the later stimulation stage are mainly due to: (1) most of the fractures around the injection well have suffered damage at the current stress state; (2) fluid pressure gradient at the location of the damage front is low; (3) fluid temperature at the location of the damage front is high. Consequently, well injectivity around the injection well increase slowly.

Overall, our modeling results adequately reproduce features of the well injectivity evolution observed at well RRG-9, including the time and magnitude of well injectivity changes. After 292 days reservoir stimulation treatment, the model predicted well injectivity increases from 0.45 to 4.15 kg/(s MPa), showing significant permeability enhancement around the injection well.

4.2 Quantitative Evaluation of Reservoir Stimulation Treatment

Figure 16 shows the model predicted spatial extent of the stimulation zone after 292 days reservoir stimulation treatment. The contours of permeability change reflect an uneven enlarge distribution of permeability increase towards outside the edges of the hydro-shearing region. The maximum value of about 350 m along the maximum horizontal principal stress (NNE-direction) was observed, with a moderate extension in the vertical direction and a minimum extension along the minimum principal stress (NWW-direction). This is mainly because the planes of optimally oriented fractures are favorable for the maximum horizontal principal stress direction. It is estimated that the volume of shear failure region reaches approximately 2.2×10^{7} m^{3} (Fig. 16d).

To quantitatively evaluate the development of the EGS reservoir, the average permeability of the entire model was plotted, as shown in Fig. 17. The modeling results indicate that the average permeability increases from 1.4 to 8.4 mD

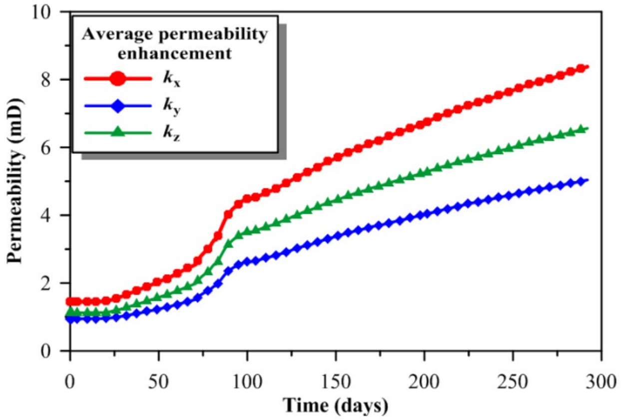

Fig. 17 Evolution of the reservoir average permeability in *x*, *y*, and *z* directions during the 292-day reservoir stimulation treatment

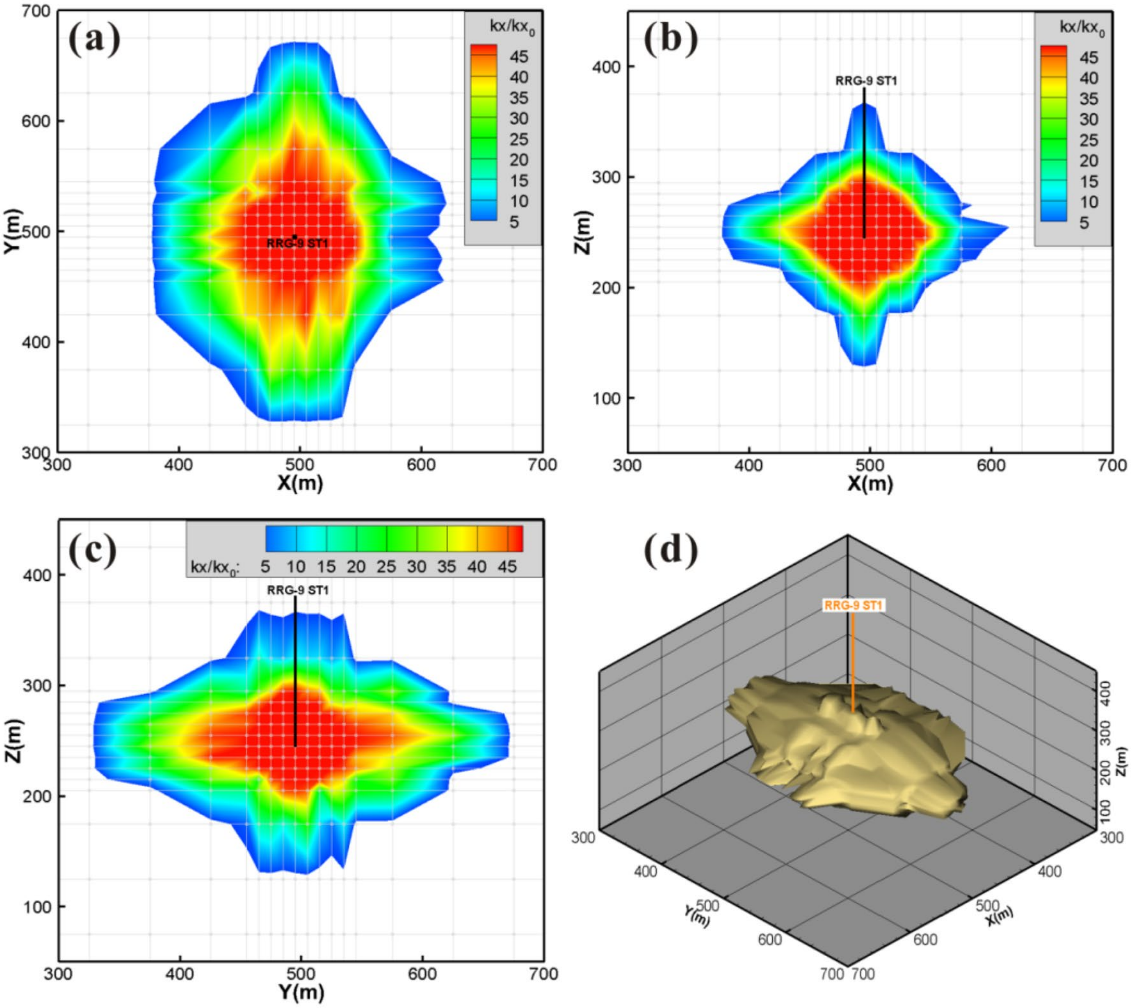

Fig. 16 Spatial extent of the predicted stimulation zone at **a** *x*–*y* plane of *z* = 250 m, **b** *x*–*z* plane of *y* = 500 m, **c** *y*–*z* plane of *x* = 500 m, and **d** three-dimensional display of the damage zone after 292 days reservoir stimulation program

along the maximum horizontal principal stress (x-axis), from 0.9 to 5.0 mD along the minimum principal stress (y-axis), and from 1.1 to 6.6 mD in the vertical direction (z-axis). For the specified extensional stress state, the model favors greatest permeability enhancement parallel to the maximum horizontal principal stress, a moderate enhancement in the vertical direction, and a smaller enhancement parallel to the minimum principal stress.

The simulated changes of injectivity are sensitive to input parameters of the THM coupled model. According to the conceptual model of fracture permeability evolution (see Sect. 2), for a general EGS system, the time at which injectivity initially begins to increase will be sensitive to: (1) the in-situ stress state, (2) material parameters present in the Mohr–Coulomb failure criterion (e.g., friction coefficient, cohesion, and shear stiffness), (3) thermoelastic rock properties (e.g., Young's modulus and coefficient of thermal expansion), (4) initial reservoir permeability (naturally fracture system), and (5) injection pressure and temperature.

For the Raft River site stimulation, many of the aforementioned parameters are constrained (see Table 4), either by the field pre-stimulation test and laboratory test results. However, it is necessary to discuss some of the more general model sensitivities, because these indicate the physical mechanisms that control fracture failure and injectivity enhancement. In fact, the effects of these parameters can be regard as the differences of hydraulic and thermal processes on the development of the EGS reservoir, such as thermoelastic rock properties control the magnitude of thermal stresses and similar to the function of injection temperature. Therefore, the knowledge of hydraulic and thermal processes on the development of the EGS reservoir is significantly important and will be discussed in detail below.

4.3 Thermal Effects on Hydro-Shearing

To determine the impact of thermal stress on EGS development, we compared the results between the HM coupled model and THM coupled model. Furthermore, the sensitivity of the thermal expansion coefficient (β_T) and injection temperature (T_{inj}) were investigated in detail. The modeling schemes are shown in Table 5. In Case c, β_T is given as 0 °C^{-1} to temporarily avoid the influence of thermal stress. The other model parameters and injection pressures are consistent with the Base case discussed in Sect. 3.

Table 5 Sensitivity analyses of thermal effects on EGS development

Number	β_T (°C^{-1})	T_{inj} (°C)
Base case	1.65×10^{-5}	50
Case a	1.65×10^{-5}	20
Case b	1.00×10^{-5}	50
Case c	0.0	50

As shown in Fig. 18, without the impacts of thermal stress (Case c), well injectivity stabilizes at a constant value without any enhancement. This indicates that changes of thermal stresses in the reservoir are the key factors for EGS reservoir growth under the hydro-shearing mechanism, which is obviously proved by the spatial distribution of effective stresses in Fig. 19. This is mainly because cold water injection along the permeable zone induces cooling shrinkage, which tends to cause a significant reduction in effective stress (Jeanne et al. 2014; Rinaldi et al. 2015; Rutqvist et al. 2015). Furthermore, permeability enhancement around the injection well gives a positive feedback for conducting cold water deeper into the reservoir deeply.

Decreasing T_{inj} from 50 (Base case) to 20 °C (Case a) results in the maximum well injectivity declining from 4.15 to 3.20 kg/(s·MPa). This is mainly because the lower temperature results in the higher viscosity and lower mobility of water, as a consequence, the effective injection rate is smaller than that with moderate injection temperature. Lower values of β_T induce smaller thermal stress. Consequently, the time that well injectivity began to enhance delays for 8 days compared with Base case. Review of Figs. 18 and 19 indicates that using subcooled water to stimulate reservoir for a long time is unfavorable to EGS development. However, using cold water to stimulate the tight reservoir in the initial stage is a good choice to improve reservoir permeability near the injection well.

4.4 Hydraulic Effects on Hydro-Shearing

To determine the impact of fluid pressure on EGS development, we performed three additional THM coupled models with different injection pressures, as shown in Table 6. In these models, the wellhead pressures keep unchanged

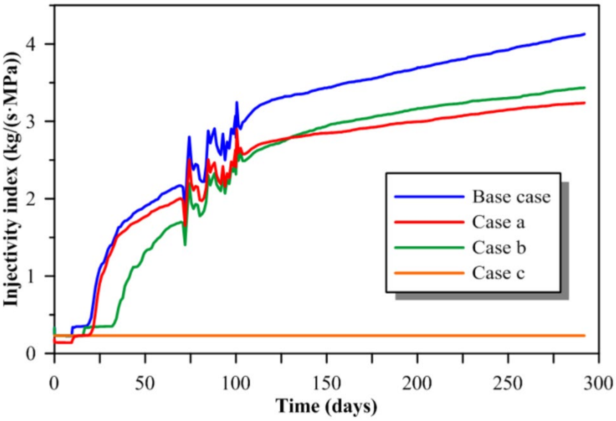

Fig. 18 Comparison of the well injectivity between THM coupled model and HM coupled model

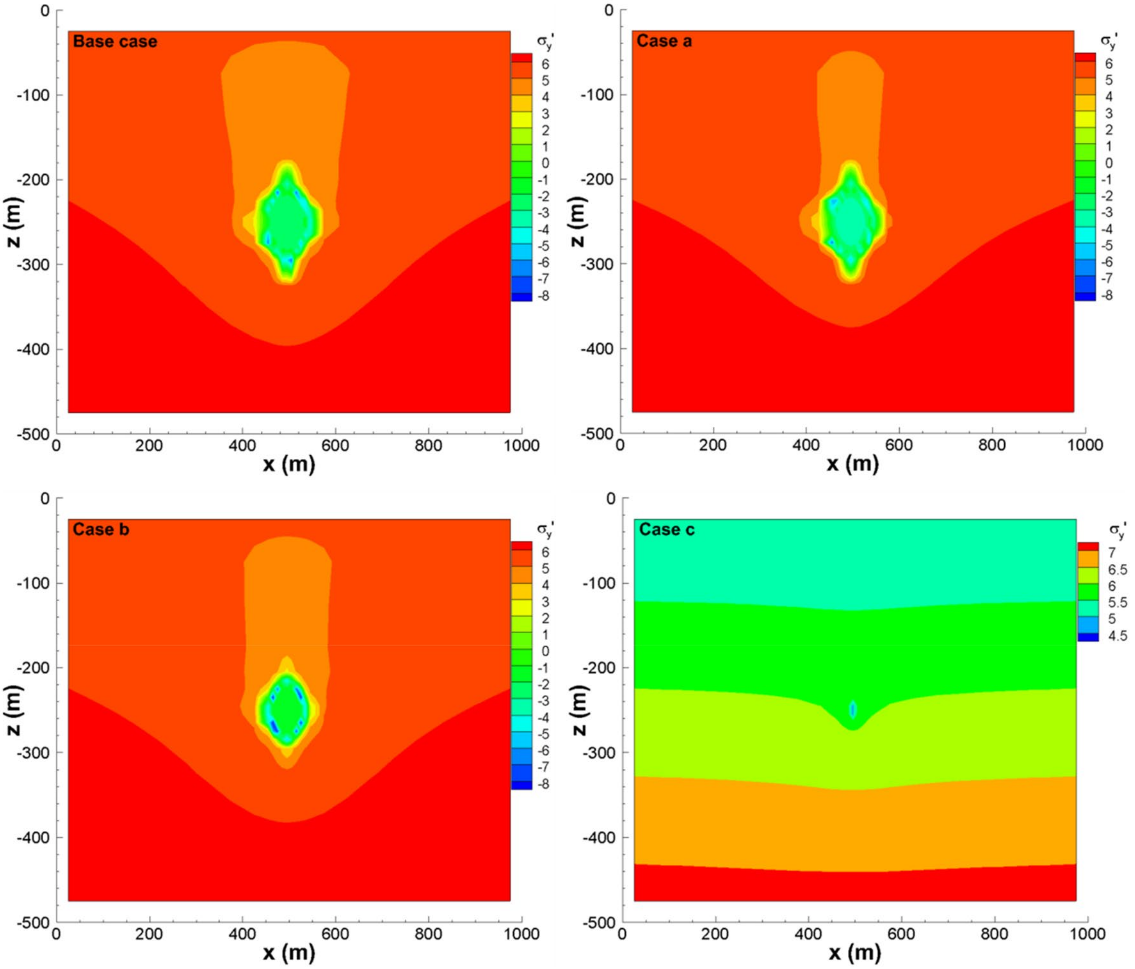

Fig. 19 Spatial distribution of the minimum principal effective stresses along the *x*–*z* plane of $y = 500$ m after 292 days reservoir stimulation treatment

Table 6 Sensitivity analyses of hydraulic effects on EGS development

Number	WHP (MPa)	T_{inj} (°C)
Case d	0.5	50
Case e	2.0	50
Case f	6.0	50

throughout the simulation run. For the convenience of comparison, all of the thermo-physical properties of the model remain constant.

Figure 20 shows the evolution of well injectivity with time under different injection pressures. Under a low injection pressure (Case d, 0.5 MPa), well injectivity began to increase on the 40th day. When increasing injection pressure

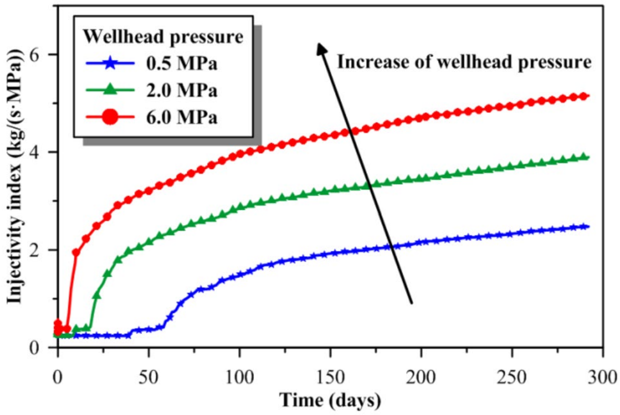

Fig. 20 Comparison of the well injectivity for different injection pressure schemes

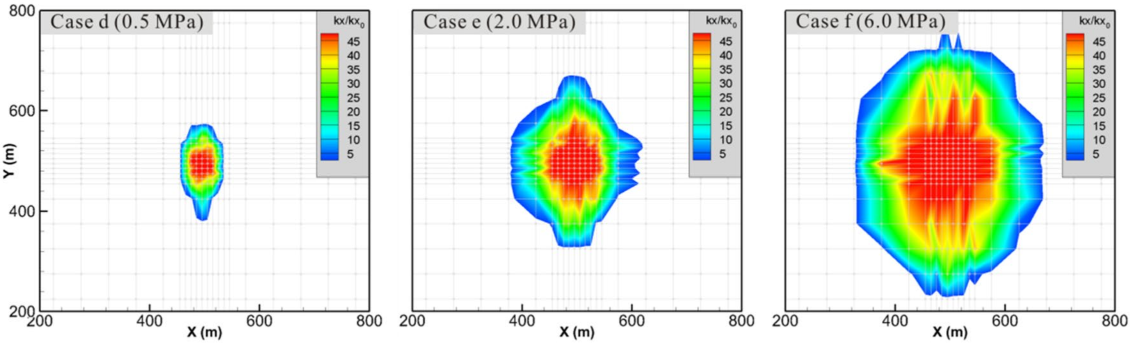

Fig. 21 Model predicted extent of the stimulation zone at the *x*–*y* plane of $z=250$ m under different wellhead pressures after 292 days stimulation program

from 0.5 to 2.0 MPa and 6.0 MPa, well injectivity began to enhances ahead of 21 days and 34 days, respectively. In addition, the resulting stimulation zone expands with the injection pressures (Fig. 21). This is because (1) the increased wellhead pressure results in significant decrease of effective stress within the reservoir and promotes shear failure of pre-existing fractures; (2) the increased pressure gradient can effectively transport cold water enters further into the hot reservoir deeply and amplify the stimulation zone.

In summary, the 3D thermo–hydro–mechanical coupling simulation results indicate that the permeability enhancement of fractured geothermal reservoir is mainly caused by the combined effects of injection-induced cooling and pressure increase. Shearing reactivation on existing fractures is mainly driven by thermal stresses superimposed on the ambient stress state under the hydro-shearing mechanism (i.e., the injection pressure is lower than the magnitude of the minimum principal stress). However, a moderate injection pressure is required to promote shear failure of existing fractures and amplify the stimulation zone.

5 Conclusions

Shear stimulation of pre-existing fractures is an effective method for improving the reservoir permeability to create an Enhanced Geothermal System (EGS). To accurately evaluate the injectivity enhancement during reservoir stimulation, we employed sub-grid-scale fracture populations that are assessed for Mohr–Coulomb failure. In addition, an empirical relationship derived from the hydro-mechanical coupled laboratory experiments was used to calculate the enhancement of fracture permeability. These complex processes have been successfully integrated into the thermo-hydro-mechanical coupled simulator TOUGH2Biot to model the changes in reservoir permeability and well injectivity associated with shear failure of pre-existing fractures in the geothermal reservoir.

The Raft River EGS demonstration project designed to develop new techniques for improving the reservoir permeability through cold-water injection. Several specified injection strategies have been employed at the target geothermal well RRG-9 with varying injection pressures and temperatures. Wellhead pressures, injection rates and fluid temperatures were continuously measured during reservoir stimulation. We have performed a series of 3D coupled thermo-hydro-mechanical simulations to study the effects of hydraulic and thermal processes on the development of the Raft River EGS project. The model was calibrated to reproduce reasonably with the field monitoring data. In particular, the validated model was used to predict the injection-induced permeability enhancement and the spatial extent of the stimulation zone.

Our simulations adequately reproduce the features of well injectivity evolution observed at the stimulation well RRG-9, including the time and magnitude of well injectivity changes. After 292 days reservoir stimulation treatment, the model predicted the stimulation zone with a volume of approximately 0.02 km^3. For the specified extensional stress state, the greatest permeability enhancement occurs along the maximum horizontal principal stress, a moderate enhancement in the vertical direction, and a smaller enhancement parallel to the minimum principal stress. The modeling results indicate that the favorable direction for the placement of production/injection wells is NNE-direction, with the maximum distance of approximately 350 m after the specified injection schedule. Additionally, the primary mechanism responsible for the EGS development into the fractured geothermal reservoir is shear failure of pre-existing fractures caused by the combined effects of injection-induced cooling and pressure increase.

Acknowledgements This work was supported by the National Key R&D Program of China (Grant 2018YFE0111300) and China Postdoctoral Science Founded Project (Grant 2019M661213). This research has also been funded by the Key Laboratory of Groundwater Resources and Environment and the Engineering Research Center of Geothermal

Resources Development Technology and Equipment, Ministry of Education, Jilin University.

References

Ayling B, Moore J (2013) Fluid geochemistry at the Raft River geothermal field, Idaho, USA: new data and hydrogeological implications. Geothermics 47:116–126

Bahrami D, Danko G, Fu PC, Guo B, Podgorney R, White M, Xia YD (2015) Poroelastic and self-propped single fracture THM models for EGS studies. In: Proceedings of the 40th workshop on geothermal reservoir engineering, Stanford, CA, 26–28 Jan 2015

Bai M, Meng F, Elsworth D, Roegiers JC (1999) Analysis of stress-dependent permeability in nonorthogonal flow and deformation fields. Rock Mech Rock Eng 32:195–219

Bradford J, Ohren M, Osborn WL, McLennan J, Moore J, Podgorney R (2014) Thermal stimulation and injectivity testing at Raft River, ID EGS Site. In: Proceedings of the 39th workshop on geothermal reservoir engineering, Stanford, CA, 24–26 Feb 2014

Bradford J, McLennan J, Moore J, Podgorney R, Plummer M, Nash G (2017) Analysis of the thermal and hydraulic stimulation program at raft river. Idaho Rock Mech Rock Eng 50:1279–1287

Bradford J, McLennan J, Moore J, Glasby D, Waters D, Kruwell R, Bailey A, Rickard W, Bloomfield K, King D (2013) Recent developments at the Raft River geothermal field. In: Proceedings of the 38th workshop on geothermal reservoir engineering, Stanford, CA 2013

Bradford J, Moore J, Ohren M, McLennan J, Osborn WL, Majer E, Nash G, Podgorney R, Freifeld B, Nye R, Rickard W, Waters D, Glaspey D (2015) Recent thermal and hydraulic stimulation results at Raft River, ID EGS Site. In: Proceedings of the 40th workshop on geothermal reservoir engineering, Stanford, CA, 26–28 Jan 2015

Breede K, Dzebisashvili K, Liu X, Falcone G (2013) A systematic review of enhanced (or engineered) geothermal systems: past, present and future. Geotherm Energy 1(4):1–27

Clark C, Sullivan J, Harto C, Han J, Wang M (2012) Life cycle environmental impacts of geothermal systems. In: Proceedings of the 37th workshop on geothermal reservoir engineering, Stanford, CA, 30 Jan–1 Feb 2012

Dempsey D, Kelkar S, Lewis K, Hickman S, Davatzes N, Moos D, Zemach E (2013) Modeling shear stimulation of the Desert Peak EGS well 27–15 using a coupled thermal-hydrological-mechanical simulator. In: Proceedings of 47th U.S. rock mechanics/geomechanics symposium, San Francisco, 23–26 June 2013

Diek A, White L, Roegiers JC, Moore J, McLennan D (2012) Borehole preconditioning of geothermal wells for enhanced geothermal system reservoir development. In: Proceedings of the 37th workshop on geothermal reservoir engineering, Stanford, CA, 30 Jan–1 Feb 2012

Freifeld B, Finsterle S (2011) Imaging fluid flow in geothermal wells using distributed thermal perturbation sensing. Lawrence Berkeley National Laboratory, University of California, Berkeley, Earth Sciences Division

Ito T, Hayashi K (2003) Role of stress-controlled flow pathways in HDR geothermal reservoirs. In: Proceedings of the thermo-hydro-mechanical coupling in fractured rock. Birkhäuser Basel, pp 1103–1124

Jaeger JC, Cook N, Zimmerman R (2007) Fundamentals of rock mechanics. 4th edn. Blackwell Publishing, Malden, MA, USA

Jeanne P, Rutqvist J, Dobson PF, Walters M, Hartline C, Garcia J (2014) The impacts of mechanical stress transfers caused by hydromechanical and thermal processes on fault stability during hydraulic stimulation in a deep geothermal reservoir. Int J Rock Mech Min Sci 72:149–163

Jones C, Moore J, Teplow W, Craig S (2011) Geology and hydrothermal alteration of the raft river geothermal system, Idaho. In: Proceedings, 36th workshop on geothermal reservoir engineering, Stanford, CA, 31 Jan–2 Feb 2011

Hossain M, Rahman M, Rahman S (2002) A shear dilation stimulation model for production enhancement from naturally fractured reservoirs. SPE J 7(2):83–195

Kelkar S, Lewis K, Hickman S, Davatzes NC, Moos D, Zyvoloski G (2012) Modeling coupled thermal–hydrological–mechanical processes during shear stimulation of an EGS well. In: Proceedings, 37th workshop on geothermal reservoir engineering, Stanford, CA, 30 Jan–1 Feb 2012

Lee HS, Cho TF (2002) Hydraulic characteristics of rough fractures in linear flow under normal and shear load. Rock Mech Rock Eng 35(4):299–318

Lei HW, Xu TF (2014) TOUGH2Biot: a coupled thermal-hydrodynamic–mechanical model for geothermal development. GRC paper, Vol. 38

Lei HW, Xu TF, Jin GR (2015) TOUGH2Biot—a simulator for coupled thermal-hydrodynamic-mechanical processes in subsurface flow systems: application to CO_2 geological storage and geothermal development. Comput Geosci 77:8–19

Majer EL, Baria R, Stark M, Oates S, Bommer J, Smith B, Asanuma H (2007) Induced seismicity associated with enhanced geothermal systems. Geothermics 36(3):185–222

McClure MW, Horne RN (2012) Investigation of injection-induced seismicity using a coupled fluid flow and rate/state friction model. In: Proceedings of the 37th workshop on geothermal reservoir engineering, Stanford, CA, 1–2 Feb 2012

McGarr A (1999) On relating apparent stress to the stress causing earthquake fault slip. J Geophys Res 104:3003–3011

MIT (2006) The future of geothermal energy: impact of enhanced geothermal systems (EGS) on the United States in the 21st Century. Massachusetts Institute of Technology, Cambridge, p 372

Pan L, Oldenburg CM, Wu YS, Pruess K (2011) T2Well/ECO2N version 1.0: multiphase and non-isothermal model for coupled wellbore-reservoir flow of carbon dioxide and variable salinity water. Earth Sciences Division, Lawrence Berkeley National Laboratory

Pandey SN, Vishal V, Chaudhuri A (2018) Geothermal reservoir modeling in a coupled thermo-hydro-mechanical-chemical approach: a review. Earth Sci Rev 185:1157–1169

Pine RJ, Batchelor AS (1984) Downward migration of shearing in jointed rock during hydraulic injections. Int J Rock Mech Min Sci 21(5):249–263

Plummer M, Huang H, Podgorney R, Bradford J, Moore J (2015) Reservoir response to thermal and high-pressure well stimulation efforts at Raft River, Idaho. In: Proceedings of the 40th workshop on geothermal reservoir engineering, Stanford, CA

Plummer M, Palmer C, Podgorney R, Bradford J, Moore J (2014) Hydraulic response to thermal stimulation efforts at Raft River based on stepped rate injection testing. In: Proceedings of 39th workshop on geothermal reservoir engineering, Stanford, CA, 24–26 Feb 2014

Pruess K, Oldenburg C, Moridis G (1999) TOUGH2 user's guide, version 2.0. Earth Sciences Division, Lawrence Berkeley National Laboratory

Riahi A, Damjanac B (2013) Numerical study of hydro-shearing in geothermal reservoirs with a pre-existing discrete fracture network. In: Proceedings of the 38th workshop on geothermal reservoir engineering, Stanford, CA, 11–13 Feb 2013

Rinaldi AP, Rutqvist J, Sonnenthal EL, Cladouhos TT (2015) Coupled THM modeling of hydroshearing stimulation in tight fractured volcanic rock. Transp Porous Med 108:131–150

Rutqvist J (2011) Status of TOUGH-FLAC simulator and recent applications related to coupled fluid flow and crustal deformations. Comput Geosci 37:739–750

Rutqvist J, Dobson PF, Garcia J, Hartline C, Jeanne P, Oldenburg CM, Vasco DW, Walters M (2015) The Northwest Geysers EGS demonstration project, California: pre-stimulation modeling and interpretation of the stimulation. Math Geosci 47:3–29

Rutqvist J, Wu YS, Tsang CF, Bodvarsson G (2002) A modeling approach for analysis of coupled multiphase fluid flow, heat transfer, and deformation in fractured porous rock. Int J Rock Mech Min Sci 39:429–442

Wang S, Huang Z, Wu YS, Winterfeld PH, Zerpa LE (2016) A semi-analytical correlation of thermal-hydraulic-mechanical behavior of fractures and its application to modeling reservoir scale cold water injection problems in enhanced geothermal reservoirs. Geothermics 64:81–95

Xie L, Min KB (2016) Initiation and propagation of fracture shearing during hydraulic stimulation in enhanced geothermal system. Geothermics 59:107–120

Zhou ZF (2007) Theory on dynamics of fluids in fractured medium. Higher Education Press, Beijing